Design and optimization of gas-liquid vortex unit using CFD simulation

Siyuan Chen, Paulien Malego, Kevin M. Van Geem, Yi Ouyang, Geraldine J. Heynderickx*

Ghent University, Laboratory for Chemical Technology, Technologiepark 125, 9052 Gent, Belgium.

*Corresponding author:

Yi Ouyang

Laboratory for Chemical Technology, Ghent University, Belgium

Address: Technologiepark 125, B-9052 Ghent, Belgium

Tel. : +32 9 264 56 77

Yi.Ouyang@UGent.be

Keywords: Process intensification; Gas-Liquid Vortex Unit; CFD; Contact Time; Geometry optimization

Abstract:

Due to the exceptional multiphase mixing and mass transfer performance, gas-liquid vortex units (GLVUs) have great potential for solvent-based applications like CO_2 capture. The high gas flow rates needed to provide the energy input for creating the centrifugal field negatively influence the contact between phases and the efficiency of the GLVU. To address this issue, computational fluid dynamics (CFD) simulations are used to optimize the design of the GLVU geometry and its operating conditions. The gas-liquid flow characteristics, contact time and total energy consumption in different GLVU geometries are analyzed. The effects of geometrical changes including reactor shape, reactor volume and gas-liquid inlet configuration are investigated. In the optimized GLVU designs, the gas-liquid contact time is increased by more than a factor of 3, while the energy consumption is reduced by 85% compared to the base case. Structural optimization of a GLVU is an effective route to improve the gas-liquid contact time. The use of CFD significantly accelerates the optimization of the design of a GLVU geometry for subsequent manufacturing.

1. INTRODUCTION

With a total emission of 35 Gt in 2021, CO_2 is the main greenhouse gas[1]. The rise of the CO_2 concentration in the atmosphere is responsible for a substantial increase of the atmospheric temperature over the past decade[2]. One option to reduce emissions to the atmosphere is to capture CO_2 from point sources and then store it, so-called CO_2 capture and storage (CCS). Therefore, it is urgent and necessary to develop stable, safe and environment-friendly approaches for CO_2 capture[3]. A commonly used CCS technology is the conventional absorber/desorber configuration, which uses amines as a solvent to capture CO_2 from the point source and strips the concentrated CO_2 from the absorbent. These gas-liquid contactors operating in the gravitational field require large volumes to handle enormous flows such as those coming from a steel mill. One of the main reasons for this is the limited mass transfer efficiency. In other words, mass transfer limitations hinder CO_2 capture performance and efficiency[4, 5].

Process Intensification (PI) refers to the improvement of processes at the operational, functional, and/or phenomena levels in a unit. This can be achieved through the integration of unit operations, the integration of functions and phenomena, or by specifically enhancing the phenomena for a set of target operations[6]. PI technology can thus result in substantially smaller, cleaner and more energy-efficient processes, and is as such playing an increasingly larger role in the chemical industry[5, 7, 8]. One way to achieve PI in chemical and other industries is the implementation of new reactor technologies. One example is the application of vortex technology. Gas-solid vortex units (GSVUs) have recently been used for different gas-solid applications including combustion[9], fluid catalytic cracking[10], drying[11, 12], biomass pyrolysis[13, 14] and oxidative coupling of methane[15, 16]. The positive PI results obtained when using vortex units for different gas-solid applications raise interest in extending the use of vortex technology

to gas-liquid applications. The resulting gas-liquid reactor is referred to as a gas-liquid vortex unit (GLVU). Voinov et al.[17-19] studied the gas-liquid hydrodynamics in a rotating gas-liquid layer. The interfacial area in the vortex bubbling layer was found to vary in the range of 1800-3000 m^{-1}. Previous research [20] experimentally studied liquid hydrodynamics in a GLVU using a high-speed camera. Over a wide operating window, the formation of gas bubbles and liquid ligaments was observed. The micromixing characteristic time and the liquid side mass transfer coefficient were calculated to be in the range of 1 - 3 ms and 1×10^{-3} - 2×10^{-3} m/s, respectively[20, 21]. More recently, the interphase mass transfer efficiency in a GLVU was evaluated by studying the chemisorption of CO_2 in a NaOH solvent[4]. It was found that the effective specific interfacial area in the GLVU varies in the range of 860 - 2750 m^2/m^3 while the range of the volumetric mass transfer coefficient was 1 - 10 s^{-1}. These values confirm the high mass transfer efficiency and mixing efficiency in a GLVU. In Figure 1, the original vortex chamber of the GLVU is presented. Tangential inlet slots are positioned on the circumferential wall of a reactor chamber to direct the gas flow into the reactor. The momentum of the gas is partially transferred to the liquid that is injected via a single liquid inlet in the top plate of the chamber creating a highly turbulent rotation of the liquid phase. Consequently, a highly dispersed gas-liquid layer is formed at the circumferential wall of the chamber. Both gas and liquid leave the reactor through a central exhaust. In this reactor, a large and rapidly renewed interface area is generated, which was observed to significantly enhance the gas-liquid mass transfer performance[4, 20, 21].

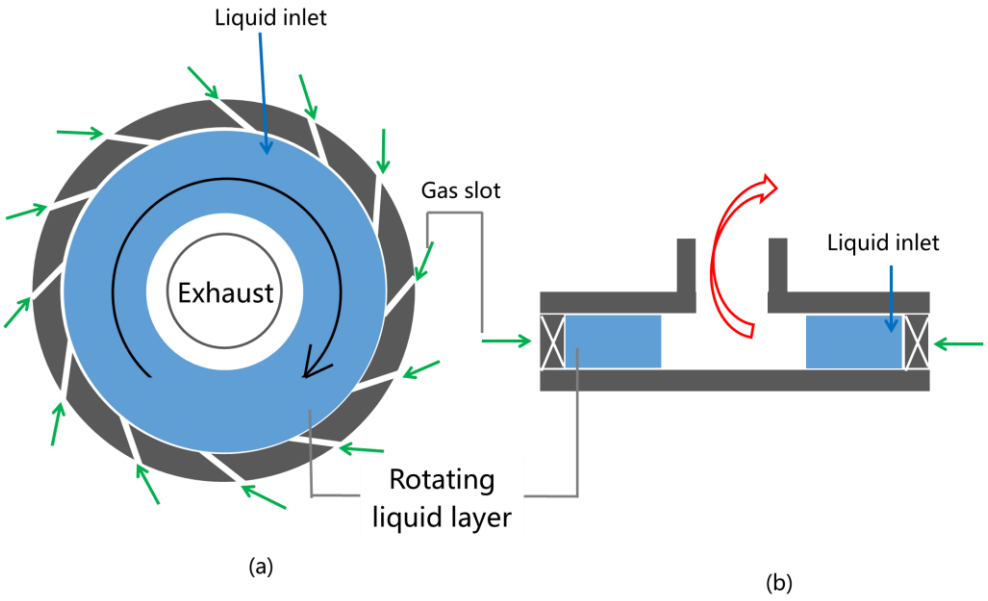

Figure 1. Schematic diagram of the GLVU : (a) top view; (b) side view. Reproduced with permission from the references [20]. Copyright 2021 Elsevier Ltd. Reproduced with permission from the reference[21]. Copyright 2021 John Wiley and Sons.

In the context of CO_2 capture, the large gas-liquid interface combined with a long contact time is essential to realize a high CO_2 absorption efficiency, especially when processing large liquid flows in industrial processes. In some literature[22-24], the low gas-liquid contact time due to large flows in intensified reactors was found to result in inadequate absorption of CO_2 and thus a lower CO_2 removal efficiency. Simply reducing the gas and liquid flows to enhance the contact time is detrimental when the goal is to realize PI since this change will decrease the vortex intensity in the GLVU[20, 25]. The operating cost of the GLVU is primarily dominated by the high flow rates required to create a uniform gas-liquid layer and to facilitate the rotation of the gas-liquid layer[4]. Therefore, it is worthwhile to investigate how to design and optimize the GLVU geometry to increase the contact time and decrease the energy consumption while maintaining the vortex flow and achieving a large and uniform gas-liquid layer.

An experimental semi-empirical approach in reactor design is extremely time-consuming and costly[26]. An economical and efficient alternative is the use of computational fluid dynamics (CFD). CFD allows to generate data and images that give detailed insights in hydrodynamics to help analyze the complex flow behavior of various physical and chemical processes. Some studies have reported the application of CFD in the design of gas-liquid reactors with a rotating gas-liquid layer[25, 27-30]. Wu et al.[31] investigated the hydrodynamics and mass transfer in a rotating packed bed (RPB) with multiple liquid inlets using a CFD model. It was found that the use of multiple liquid inlets is beneficial for PI as it improves the gas-liquid mass transfer efficiency. Li et al.[32] implemented 3D Eulerian multiphase simulations to study the liquid hydrodynamics in a novel disk-distributor RPB. They found that the use of the disk-distributor remarkably increases the liquid holdup, residence time and wetting efficiency of a high-viscosity liquid in the packing zone. Su et al.[28] improved the circulation of a liquid flow in an RPB with internal circulation by structure optimization.

In our previous work[25], CFD simulations were already performed to study hydrodynamics and mixing efficiency in a GLVU. In addition, the results demonstrated that the use of multiple liquid inlets will result in a more uniform liquid velocity distribution in the GLVU. The applied CFD model was validated[25] and is therefore used in the present work. The applied model assures that the numerical approach for problems involving complex geometries and multiphase flows is satisfactory and reliable. In the present work, different GLVU geometries are designed and studied, with the goal of improving the gas-liquid contact time and decreasing energy consumption. These improvements will result in an increase in gas-liquid mass transfer efficiency. The effects of different geometries on the gas-liquid contact time and dispersion inside the vortex chamber are studied using CFD simulations. Additionally, the energy consumption of the resulting GLVU designs is evaluated. The presented results set out the initial

guidelines along which new GLVU geometries can be designed and optimized before being built. A number of selected geometries will be constructed and used in future experimental work on CO_2 capture.

2. REACTOR GEOMETRY

The geometry of the GLVU reactor used in this work as a reference was elaborated in detail in the work of Ouyang et al.[20, 21]. As such, only a brief description of the GLVU geometry is given. The base case GLVU geometry, containing a cylindrical vortex chamber, a central exhaust, 12 tangentially inclined gas inlet slots and a liquid inlet, is shown in Figure 2. The vortex chamber has a diameter of 80 mm and a height of 15 mm. The exhaust in the top plate has a diameter of 20 mm. The 12 gas inlet slots have a width of 0.65 mm and are equally distributed over the circumferential wall of the vortex chamber, inclined tangentially at an angle of 10 °. The liquid is introduced through a single inlet with a diameter of 4 mm in the top plate of the chamber. A rotating gas–liquid layer in bubbly flow condition is formed near the circumferential wall of the vortex chamber. Operating in a centrifugal field was already found to result in the intensification of the gas-liquid mass and heat transfer in the vortex unit[4, 20, 21, 25]. In this work, a number of new GLVU geometries are proposed and studied numerically. The contact time between the gas phase and the liquid phase in the proposed GLVU geometries is compared with that in the base case GLVU.

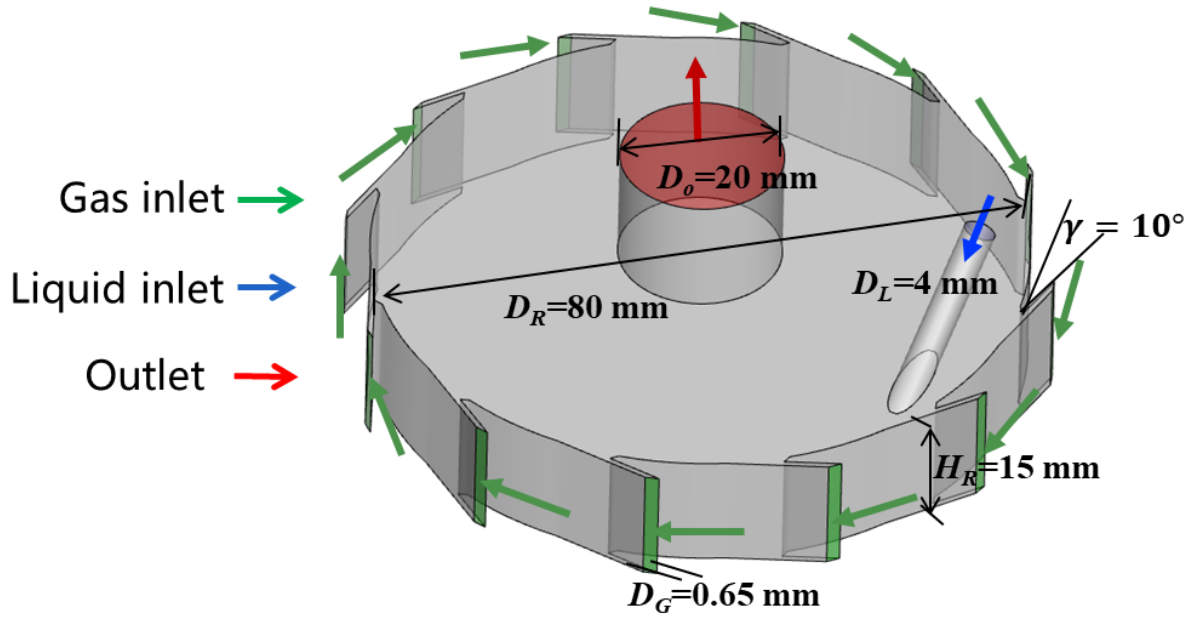

Figure 2. Schematic diagram of the GLVU (base case) for CFD simulation

3. NUMERICAL MODEL

3.1. GOVERNING EQUATIONS

The volume of fluid (VOF) model and the Eulerian-Eulerian two-fluid model are most often applied in multiphase flow simulations. The interface between a gas phase and a liquid phase can be effectively monitored using the VOF model[33-35]. However, a fine grid and a small time-step are required to accurately describe the gas-liquid interface. The consequence is a highly time-consuming simulation if applied to a gas-liquid mixture in a bubbly flow rotating at a high velocity for which phase interaction is high[36-38]. In contrast, the Eulerian-Eulerian two-fluid model has the potential to reduce the required simulation time as a more coarse grid and a higher simulation time step can be used. It has already been confirmed that the Eulerian-Eulerian two-fluid model is a powerful tool to predict the hydrodynamics of gas-liquid mixtures rotating in reactors such as RPBs[24, 39, 40] and GLVUs[25]. Therefore, the Eulerian-Eulerian two-fluid model is applied to the numerical simulations in the present work.

Detailed discussions and descriptions of the Eulerian-Eulerian two-fluid model can be found in various recent publications[25, 39, 41-43]. Therefore, only a brief summary of the most relevant equations to be solved is given. Assuming that gas and liquid are incompressible and immiscible, the mass conservation equation for phase q is[44]:

$$\frac{\partial}{\partial t}\left(\alpha_q \rho_q\right) + \nabla \cdot \left(\alpha_q \rho_q \overrightarrow{u_q}\right) = 0 \tag{1}$$

where α_q, $\overrightarrow{u_q}$ and ρ_q are the volume fraction, velocity and density of fluid phase q, i.e., liquid or gas, respectively. At any spatial location, the gas volume fraction and the liquid volume fraction sum up to 1.

The momentum equation for phase q is expressed as[44]:

$$\frac{\partial}{\partial t}\left(\alpha_q \rho_q \vec{u}_q\right) + \nabla \cdot \left(\alpha_q \rho_q \overrightarrow{u_q} \overrightarrow{u_q}\right) = -\alpha_q \nabla p + \overrightarrow{F_{G-L}} - \nabla \cdot \overline{\tau_q} + \alpha_q \rho_q g \tag{2}$$

where p represents pressure, g is the gravitational acceleration, $\alpha_q \nabla p$ is the pressure gradient and $\overline{\tau_q}$ is the viscous stress-strain tensor. As a consequence of the high-speed rotation of the gas-liquid layer and the strong interactions between phases in the GLVU[4, 20, 21], the overall interphase forces $\overrightarrow{F_{G-L}}$ to be considered are drag, lift, and turbulent dispersion forces between the gas phase and the liquid phase. The drag force is often regarded as the most important interphase force[45-47]. In this work, only the drag force is taken into consideration [46, 47]:

$$\overrightarrow{F_{G-L}} = K_{G-L}(\overrightarrow{u_G} - \overrightarrow{u_L}) \tag{3}$$

where K_{G-L} is the interfacial momentum exchange coefficient, which are calculated by :

$$K_{G-L} = \frac{3}{4}\rho_L \alpha_G \alpha_L \frac{C_D}{d_b}|\vec{u}_G - \vec{u}_L| \tag{4}$$

where d is the bubble diameter. The bubble diameter can either be imposed (as a fixed bubble size)[48, 49] or calculated from a Population Balance Model (PBM)[50, 51], which predicts the bubble size distribution. Scargiali et al.[52] performed simulations in a gas-liquid reactor applying two bubble sizes, 2 mm and 4 mm. Their results indicate that bubble size had only a minor influence on variables like total gas holdup and its distribution. It implies that the gas-liquid

hydrodynamics in the reactor are not substantially affected by changing the bubble size. Moudoud et al.[53] arrived at similar conclusions in their studies. Based on the experimental work of Ouyang et al.[4], the bubble diameter is set at 1.5 mm in the present work. Assuming a fixed bubble size based on experimental data is also a conventional approach for an E-E simulation[54]. Consequently, a more in-depth exploration of the effects of bubble coalescence and breakage on gas-liquid hydrodynamics and mass transfer using a CFD-PBM simulation will be the focus of our subsequent studies. C_D represents the drag coefficient. For the calculation of the drag coefficient, the correlation of Ishii-Zuber is used[55]:

$$C_D = max\left(\frac{24}{Re_b}(1 + 0.15Re_b^{0.687}), min\left(\frac{2}{3}Eo^{1/2}, \frac{8}{3}\right)\right) \quad (5)$$

The Eötvös number *Eo* used in the drag correlation is defined as:

$$Eo = \frac{g(\rho_L - \rho_G)d^2}{\sigma} \quad (6)$$

The swirling flow in a GLVU is highly turbulent. There is no unified turbulence model to describe the turbulent characteristics of a rotating gas-liquid mixture. Different turbulence models, such as the k-ε model, the renormalization group (RNG) k-ε model, the k-ω model, and the shear stress transport (SST) *k-ω* model have been evaluated for simulation of a swirling flow by Maluta et al.[56], Zhang et al.[57] and Putra et al.[58]. The results showed that the SST k-ω model shows a better performance compared to other turbulence models. This is due to its ability to accurately predict flow separation for adverse pressure gradient conditions. Therefore, the SST k-ω turbulence model is adopted. The equations are found in Equations (7) and (8)[59]:

$$\frac{\partial}{\partial t}(\rho_q k_q) + \frac{\partial}{\partial x_j}(\rho_q k_q u_{j,q}) = \frac{\partial}{\partial x_j}(\Gamma_{k,q}\frac{\partial \omega_q}{\partial x_j}) + \tilde{G}_{k,q} - Y_{k,q} + S_{k,q} \quad (7)$$

$$\frac{\partial}{\partial t}(\rho_q \omega_q) + \frac{\partial}{\partial x_j}(\rho_q \omega_q u_{j,q}) = \frac{\partial}{\partial x_j}(\Gamma_{\omega,q}\frac{\partial \omega_q}{\partial x_j}) + G_{\omega,q} - Y_{\omega,q} + D_{\omega,q} + S_{\omega,q} \quad (8)$$

In these equations, k and ω denote the turbulence kinetic energy and specific dissipation rate, respectively. Γ, G, Y and S represent the generation, diffusivity, dissipation and source terms, respectively. $D_{\omega,q}$ represents the cross-diffusion term. The subscript q refers to both phases.

The effective diffusivities used in the SST k-ω turbulence model are calculated by:

$$\Gamma_{k,q} = \mu_q + \frac{\mu_{t,q}}{\sigma_{k,q}} \tag{9}$$

$$\Gamma_{\omega,q} = \mu_q + \frac{\mu_{t,q}}{\sigma_{\omega,q}} \tag{10}$$

where $\sigma_{k,q}$ and $\sigma_{\omega,q}$ are the turbulent Prandtl numbers for k and ω, respectively. The turbulent viscosity, $\mu_{t,q}$, is computed as follows:

$$\mu_{t,q} = \frac{\rho k_q}{\omega_q} \frac{1}{\max[\frac{1}{\alpha^*}, \frac{S' F_2}{a_1 \omega_q}]} \tag{11}$$

where α^* is a coefficient that dampens the turbulent viscosity causing a low-Reynolds number correction; a_1 is the model constant and equals 0.31; F_2 is a function that is 1 for boundary-layer flows and 0 for free shear layers, respectively. The strain rate magnitude $S'$is defined as:

$$S' = \sqrt{2 S_{ij} S_{ij}} \tag{12}$$

$$S'_{ij} = \frac{1}{2}\left(\frac{\partial u_i}{\partial x_j} + \frac{\partial u_j}{\partial x_i}\right) \tag{13}$$

The Troshko-Hassan formulation[60] is used to incorporate the effect of the gas turbulence on the hydrodynamics as suggested by Zhang et al.[61]. The formulation can be expressed as follows:

$$S_{k,q} = 0.75\ \alpha_q K_{G-L} |\vec{u}_G - \vec{u}_L|^2 \tag{14}$$

$$S_{\omega,q} = \frac{0.45 \frac{1}{\tau_p} S_{k,q}}{C_\mu k_q} - \frac{\omega S_{k,q}}{k_q} \tag{15}$$

where the model constant C_μ equals 0.09 and τ_p is the characteristic time of the induced turbulence defined as:

$$\tau_p = \frac{d_p}{3 C_D |\vec{u}_G - \vec{u}_L|} \tag{16}$$

The numerical model was previously found to accurately simulate the base case GLVU used in this work[25]. The validation was performed through a comprehensive comparison of experimentally and numerically obtained values for the pressure drop over the gas-liquid layer and the liquid velocity on the bottom plate of the chamber. A good quantitative agreement was observed over a wide range of GLVU operating conditions. The validated numerical model is applied in this study.

3.2. Boundary Conditions and Numerical Settings

The simulated geometry (*Base case*) shown in Figure 2 is a slightly simplified representation of the complete experimental setup. To save calculation time and cost, the simulated geometry contains only the vortex chamber, the liquid inlets, the gas inlets and the exhaust. The results of previous work[25] have proven that this simplified approach is feasible. At the outlet of the GLVU, atmospheric pressure is imposed. A no-slip boundary condition is specified for all chamber walls. The velocity-inlet type condition is adopted for the gas inlet flow and liquid inlet flow with α_G=1.0 and α_L=1.0, respectively. Table 1 summarizes the boundary conditions and the physical properties of both phases used in the simulations.

The computational domain is discretized using hexahedral structured grid cells. A grid selectivity study, which is discussed in previous work[25], was conducted. The selected grid size of 2 mm remains unchanged for all GLVU geometries used in the optimization study.

All simulations are performed using the commercial software, ANSYS Fluent 2021R2®. The Phase Coupled Semi-Implicit Method for Pressure-Linked Equations (SIMPLE) scheme[62] is employed to solve the pressure-velocity coupled equations. A first-order upwind algorithm is adopted to solve all equations. The convergence criterion for all equations is set at 10^{-3}. The simulation is initialized by feeding only gas (air) to the empty chamber. Once a steady gas flow

field is obtained, the liquid phase (water) is fed to the chamber too. Both the gas and liquid leave the vortex chamber via the central exhaust. During a simulation, the volume-averaged liquid volume fraction in the grid cells of the vortex chamber is monitored as a function of time. When the monitored value remains constant or fluctuates regularly over time, the simulation is stopped and a time-averaging of all flow characteristics is performed.

Table 1. *Boundary conditions and fluid physical properties*

Description	Value
Wall boundary condition	No slip
Inlet boundary condition	Velocity inlet
Outlet boundary condition	Pressure outlet
Gas phase	Air
Gas density (kg/m^3)	1.225
Gas viscosity (mPa·s)	1.78×10^{-2}
Liquid phase	Water
Liquid density (kg/m^3)	998
Liquid viscosity (mPa·s)	1
Temperature (K)	293.15

3.3. ASSESSMENT OF HYDRODYNAMIC PERFORMANCE

3.3.1. Contact time assessment

A schematic representation of the gas-liquid layer in the vortex chamber is given in Figure 3. This bubbly flow was experimentally observed[20]. The gas-liquid mass transfer inside the chamber was already confirmed to mainly occur in the gas-liquid layer[4, 20, 25]. In the present study, the range of the gas-liquid volumetric flow ratio is between 70 and 700 (with a gas flow

rate of 25 to 75 Nm^3/h and a liquid flow rate of 110 to 330 kg/h). In the region between the gas inlet and the central outlet, a stable rotating gas-liquid layer is formed due to the momentum transfer from the gas phase to the liquid phase. As a result, the liquid volume fraction in this area is high. However, near the outlet, this stable gas-liquid layer disappears, leading to the liquid volume fraction falling within the range of 0 to 0.1. This behavior is directly related to the aforementioned range of the gas-liquid volumetric flow ratio. This observation is also in alignment with the experimental findings[20]. Therefore, employing the contact time as a metric to evaluate the hydrodynamic performance of the GLVU is justified. The contact time, representing the time needed for the gas to flow through the gas-liquid layer, can be calculated from the following equation.

$$t_c = \frac{V_{G-L}\,\varepsilon_G}{Q_G} \tag{17}$$

$V_{G\text{-}L}$ is the volume of the gas-liquid layer near the wall of the vortex chamber, indicated by the colored zone in Figure 3. The average gas volume fraction in the gas-liquid layer (ε_G) corresponds to the fraction of gas bubbles in that layer, indicated in yellow in Figure 3. Q_G represents the rate of the gas flow fed to the GLVU. The calculated value (t_c) is used to evaluate the gas-liquid contact time in the GLVU. The values of $V_{G\text{-}L}$ and ε_G used in Eq. (6) are determined based on the simulation results that provide the liquid volume fraction value in each grid cell. When the (time-averaged) liquid volume fraction of a grid cell is calculated to have a value between 0.1 and 0.9, the cell is assumed to be part of the gas-liquid layer. Theoretically, these specific criteria will not affect the comparison of different GLVU designs as long as the same criteria are used for all cases. For one of the simulated geometries, the result of this approach is presented in Figure 4, where the calculated liquid volume fractions (Figure 4(a)) in the different cells are processed to the liquid layer volume ($V_{G\text{-}L}$) as shown (the colored region in Figure 4(b)). The average gas fraction ($\varepsilon_G = 1 - \varepsilon_L$) in the gas-liquid layer is the volume-averaged value over all selected cells.

The gas residence time distribution stands as one of the crucial metrics in evaluating the hydrodynamic performance of reactors. For all the cases studied in this work, a detailed comparison between the mean gas residence time and contact time is found in the Supporting Information. Additionally, it is discussed why the contact time rather than the mean gas residence time is preferred as the primary assessment criterion to evaluate the reactor hydrodynamic performance. In short, the mean gas residence time is higher than the contact time because it considers gas flow through the entire reactor, while the contact time measures gas flow through the gas-liquid layer only. The gas-liquid volume is always smaller than that of the whole reactor because there is no stable gas-liquid layer in the center of the vortex chamber (see Figure 4). Furthermore, the contact time more accurately reflects the state of gas-liquid flow within the chamber. Therefore, the selection of the contact time as the principal metric better aligns with this study's focus on gas-liquid flow behavior.

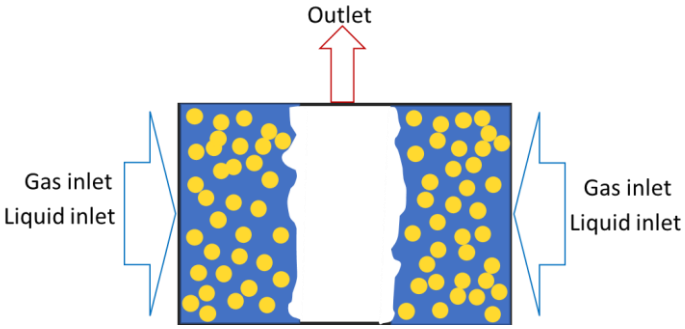

Figure 3. Schematic representation of the gas-liquid layer in the vortex chamber. Blue represents the liquid phase in the gas-liquid layer, while yellow represents the gas bubbles in the gas-liquid layer.

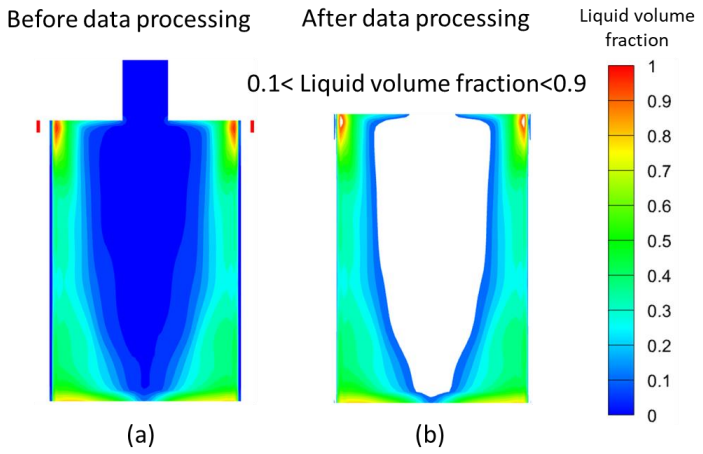

Figure 4. Processing of a liquid volume fraction contour: (a) before data processing, (b) visualization of cells with a liquid volume fraction between 0.1 and 0.9, i.e. the so-called gas-liquid layer volume used in this work

3.3.2. Energy consumption assessment

It is important to examine the energy efficiency of the designed GLVR. The gas flow serves as the primary source of energy input in the vortex chamber, driving the rotation of the gas-liquid layer. The total energy consumption per unit liquid holdup volume can be calculated as follows:

$$E_{\text{total}} = \frac{W_{\text{input}}}{V_{G-L}\varepsilon_L} \tag{18}$$

Where W_{input} represents the total energy input power. Based on the concept that the gas flow is the primary energy input to the system, P_{input} can be determined as:

$$W_{\text{input}} = Q_G\Delta P + Q_G\rho_G\left(\frac{1}{2}v_{\text{in}}^2 - \frac{1}{2}v_{\text{out}}^2\right) \tag{19}$$

In this equation, ΔP represents the pressure drop, ρ_G is the density of the gas phase, v_{in} is the superficial gas velocity at the circumferential wall, and v_{out} is the superficial gas velocity near the center of the chamber. In Figure 5, positions I and II are measurement points for pressure and gas velocity. Position I is located near a narrow gas slot injection, while Position II is at the center of the chamber. Point I is positioned at the middle of the reactor with a radial location of (r_R -0.0005m), while Point II is located at r_o. The pressure contours for each studied cases can be found in Figure S2 in the Supporting Information.

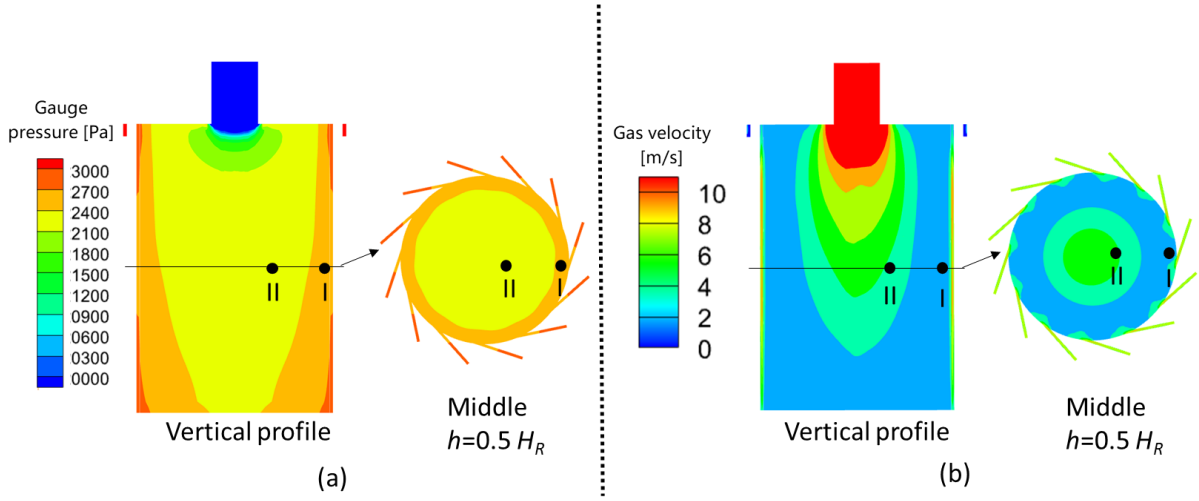

Figure 5. (a) Pressure contour in a GLVU, (b) gas velocity contour in a GLVU; I, II represent the measure points of pressure and gas velocity.

4. RESULT AND DISCUSSION

4.1. SIMULATION CASES

Multiphase flow behavior, gas-liquid contact time and energy consumption in a GLVU depend on different variables, including geometric variables, gas and liquid flow rates and physical properties of the gas and liquid phases. In this work, mainly the effects of changing geometric variables and gas-liquid flow rates are studied. The results of a selected number of all performed simulations are presented in this paper to provide guidelines for the design of a GLVU and its operating conditions. Figure 6 visualizes the GLVU geometries for which simulation results are presented in this work. The design details are summarized in Table 2. The outlet radius (r_o) for all designed GLVUs is 7.5mm. The geometric variables that are considered in the optimization study include the diameter and height of the reactor chamber (chamber shape and size) and the gas and liquid inlet configurations (gas and liquid inlet height and liquid inlet position). In our previous work, it was already demonstrated that the use of multiple liquid inlets results in a more uniform liquid velocity distribution in the vortex chamber[25]. Therefore, multiple liquid

inlets are used for each GLVU geometry in our optimization study. These tangentially inclined inlets are located in between the 12 gas inlets.

A series of transient simulations are performed, meanwhile progressively adjusting the design and/or operating conditions of the GLVU. The case-to-case modifications are carried out to improve the overall performance of GLVU. They are based on the evaluation of the results from the previous simulation cases. With a progressing number of simulation results, the gas and liquid flow rate, and the chamber volume converge towards optimal values. The performance of the original GLVU geometry (*Base case*) is studied first. The performance of the newly designed geometries with changing chamber size and inlet configurations is compared with the performance of the *Base case*. To discuss the simulation results clearly and efficiently, geometrical parameters are processed in the sequence described below. Different operation conditions are considered for changing geometries as well.

1. Chamber shape: In *Cases* 1.I, 1.II, 1.III and *Cases* 2.I, 2.II, 2.III, the chamber shape varies. In *Cases* 1.I, 1.II, 1.III, the chamber has a pancake shape, whereas in *Cases* 2.I, 2.II, 2.III, it has a cylindrical shape. It should be noted that both chambers have the same volume.

2. Chamber volume (chamber height): In *Cases* 2.I, 2.II, 2.III and *Cases* 3.I, 3.II, 3.III, the chamber height is varied. Both chambers are cylindrical and have the same diameter. The change in height results in a change in chamber volume.

3. Gas inlet height: The variation in gas inlet height and its effects are investigated in *Case* 3.III and *Case* 4. A “full gas inlet height” is set in *Case* 3. At “full gas inlet height”, the height of the slot equals the height of the chamber. A “partial gas inlet height” is set in *Case* 4. The results

of *Case* 3.III and *Case* 4 show that a full gas inlet height is necessary to have a good gas-liquid dispersion. Consequently, it is used for the subsequent geometries (*Cases* 5.I, 5.II and 5.III and *Case* 6).

4. Liquid inlet configuration (liquid inlet height and position): The effect of the liquid inlet height is investigated by comparing *Case* 2.III and *Cases* 5.I, 5.II and 5.III. A "full liquid inlet height" is used in *Case* 2.III while a "partial liquid inlet height" is applied in *Case* 5.I, *Case* 5.II and *Case* 5.III. Additionally, the position of the liquid inlet varies in *Cases* 5.I, *Case* 5.II and *Case* 5.III. They are positioned in the top, middle and bottom of the chamber in *Case* 5.I, *Case* 5.II and *Case* 5.III respectively.

5. Gas and liquid inlet width: The effect of inlet width is investigated in *Case* 5.I and *Case* 6. The inlet width is 1 mm in *Case* 5.I, while in *Case* 6 it is reduced to 0.5 mm, both for gas and liquid inflow.

For *Cases* 1, 2 and 3, the gas and liquid flow rates are varied. Based on the obtained results, a set of gas and liquid flow rates is selected to be used in *Cases* 4, 5 and 6. A complete overview is given in Table 2.

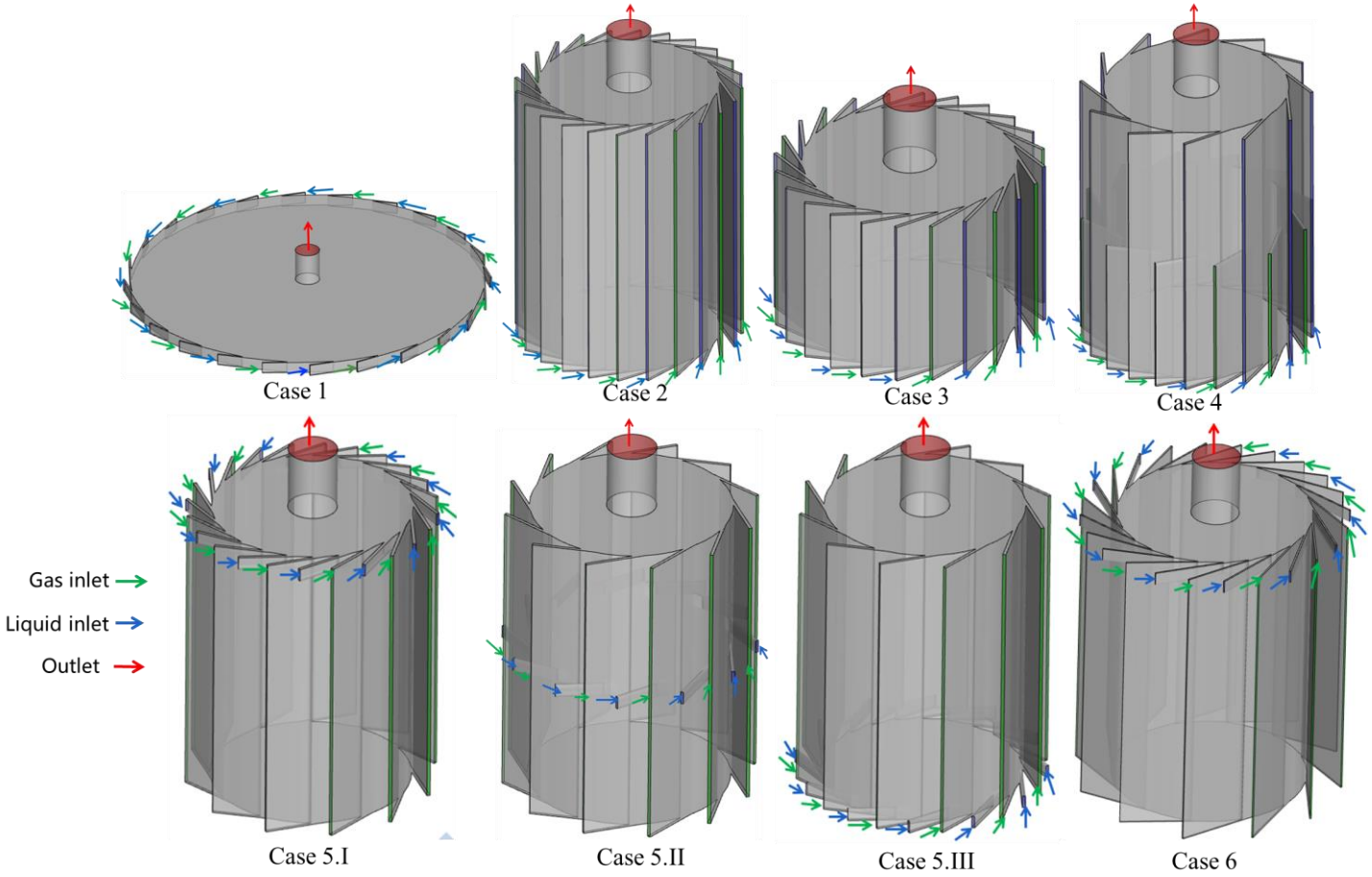

Figure 6. Schematic diagram of the optimized GLVU geometries used in different simulated cases

Table 2. *Chamber geometry parameters and inlet feed rates for different GLVU geometries*

Case	Chamber diameter/mm	Chamber height/mm	reactor volume/mL	Gas inlet height/mm	Liquid inlet height/mm	Liquid inlet position	Inlet width/mm	Gas flow rate/(m^3/h)	Liquid flow rate/(kg/h)
B.I	80	15	76	15	4*	Top plate	0.65	25	110
B.II								75	110
B.III								25	330
1.I	218	7	263	7	7	Full height	1	25	110
1.II								75	110
1.III								25	330
2.I	60	93	263	93	93	Full height	1	25	110
2.II								75	110
2.III								25	330
3.I	60	50	181	50	50	Full height	1	25	110
3.II								75	110
3.III								25	330
4	60	93	263	46.5	93	Full height	1	25	330
5.I	60	93	263	93	4	Partial height, Top	1	25	330
5.II						Partial height, middle	1		

5.III						Partial height, bottom	1		
6	60	93	263	93	4	Partial height, Top	0.5	25	330

*: For base case GLVU geometry, the liquid inlet diameter is 4 mm.

4.2. GLVU DESIGN (BASE CASE)

4.2.1. CONTACT TIME

Simulation results for the base case GLVU, with the geometry shown in Figure 2, are evaluated first as they form the starting point for the optimization of the GLVU. The geometric variables and operating conditions for *Base cases* B.I, B.II and B.III can be found in Table 2. As discussed, the gas-liquid dispersion and contact time determine the performance of the GLVU. Figure 7 shows the liquid volume fraction contours in the top, middle ($h = 0.5H_R$) and bottom of the chamber, as well as in a vertical cut of the base case GLVU, for different gas and liquid flow rates. Due to the tangential injection of air into the vortex chamber, a highly turbulent and dispersed gas-liquid mixture is formed in a strong centrifugal field. An increase in the liquid volume fraction is observed at the position of the single liquid inlet in the top plate of the chamber, resulting in a lower local circumferential uniformity of the gas-liquid layer. The non-uniformity of the liquid volume fraction contour at the top plate becomes more obvious as the liquid flow rate increases. The initial conclusion is that a GLVU with the base design is not suitable for conditions requiring a high liquid flow rate, especially those exceeding 110 kg/h. This observation aligns with previous experimental results[20].

The results for the presented *Base cases,* gathered in Figure 7(d), show the effect of changing the gas and liquid flow rates on the gas-liquid contact time for the base case GLVU design. When increasing the gas flow rate (Q_G) from 25 m^3/h to 75 m^3/h and keeping the liquid flow rate (Q_L) constant at 110 kg/h, the contact time decreases from 6.31 ms to 2.14 ms. It can be explained by the decrease in the gas-gas-liquid layer volume and the increase of the gas velocity in the vortex chamber with increasing gas flow rate. The increase in the gas flow rate by a factor of three causes a huge increase in the denominator in Eq. (6). The latter is the major contribution to the decrease in contact time. A decrease of the gas-liquid layer volume is observed in *Base*

case B.II compared to *Base case* B.I and *Base case* B.III. As explained by Ouyang et al.[20], the consequence of an increase in the gas flow rate is the formation of a strong centrifugal field and an increase of the drag force exerted on the gas-liquid layer. The competition between the centrifugal force and the drag force is found to result in a thinner gas-liquid layer. The low gas-liquid contact time in the chamber will result in issues for certain applications, such as a low CO_2 capture efficiency in the context of CCS [22-24]. When the gas flow rate is maintained constant at 25 m^3/h and the liquid flow rate is increased from 110 kg/h to 330 kg/h, the contact time increases from 6.31 ms to 6.44 ms due to an increased gas-liquid layer volume ($V_{G\text{-}L}$).

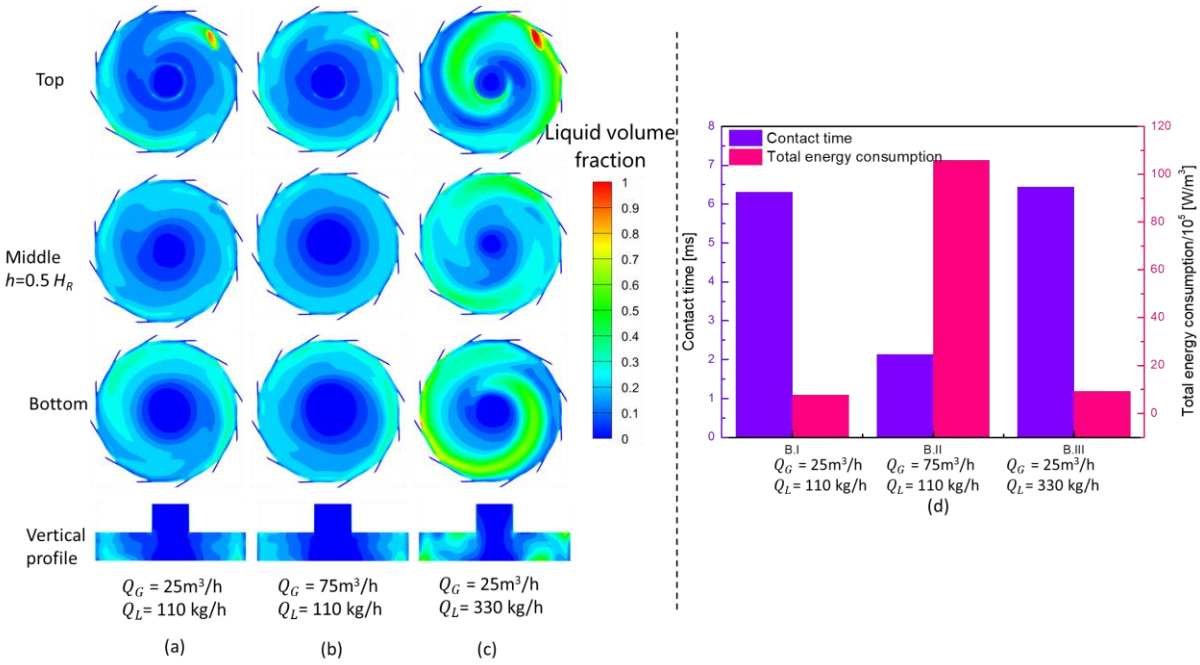

Figure 7. Liquid volume fraction contours for base case GLVU design: (a) regular flow (B.I), (b) increased gas flow (B.II), (c) increased liquid flow (B.III); (d) gas-liquid contact time and total energy dissipation for base case GLVU design.

4.2.2. ENERGY CONSUMPTION

Table S1 shows the pressure drop and energy consumption for the *Base cases* under various combinations of gas and liquid flow rates (see Supporting Information). It is noticeable that the ΔP increases as both the liquid and gas flow rates increase. The influence of the gas flow rate on ΔP is greater than that of the liquid flow rate. These results are in good agreement with

experimental data. When the gas flow rate is 25 m^3/h and the liquid flow rate is 110 kg/h, the simulation result quantitatively agrees with the experimental result. Increasing the gas flow rate leads to an increase in gas drag force and a higher momentum transfer from the gas phase to the liquid phase in the rotating gas-liquid layer, leading to a greater pressure drop. Additionally, increasing the liquid flow rate increases liquid holdup and the thickness of the gas-liquid layer in the GLVR. It implies that the gas phase needs to pass more liquid volume elements and consumes more gas momentum energy. A high-pressure drop requires more energy to overcome it. Energy consumption increases as both the liquid and gas flow rates increase, as shown in Figure 7(d).

4.3. GLVU GEOMETRY OPTIMIZATION

4.3.1. EFFECT OF CHAMBER SHAPE

The gas and liquid flow rates and the chamber volume are variables affecting the gas-liquid contact time. The chamber volume is determined by chamber height (D_H) and chamber diameter (D_R). When the chamber volume is fixed, the chamber diameter to chamber height ratio (D_R/D_H) is a good measure for the chamber shape, which will influence the hydrodynamics. The first step in the geometrical optimization of the GLVU is taken by investigating the effect of a varying chamber shape, as shown in Figure 8. In *Case* 1 and *Case* 2, two chambers with a volume higher than that of the base case design are proposed to prolong the gas-liquid contact time. The volumes of the two chambers are equal, but the chamber diameter to chamber height ratio (D_R/D_H) is 31.1 for *Case* 1 (pancake shape) and 0.645 for *Case* 2 (cylinder shape). The geometric variables and the operating condition for *Cases* 1.I, 1.II, 1.III and *Cases* 2.I, 2.II, 2.III are listed in Table 2. The dispersion of the gas-liquid layer and of the gas-liquid contact time in both chambers are compared to evaluate the efficiency of the different shapes.

Figure 8 shows the liquid volume fraction contours for the pancake-shaped chamber *Cases* 1.I, 1.II, 1.III and cylinder-shaped chamber *Cases* 2.I, 2.II, 2.III, and In Table S1 the gas-liquid layer volume and contact time for both chambers at different gas-liquid flow rates are given. For the pancake shape chamber (Figures 8(c)-7(e)), a gas-liquid layer is formed on the bottom of the chamber over the full radius. When increasing the gas flow rate from 25 m^3/h to 75 m^3/h, the liquid accumulation on the bottom of the chamber disappears due to the increased inflow of momentum. However, when increasing the liquid flow rate from 110 kg/h to 330 kg/h and maintaining the gas flow rate at 25 m^3/h, the liquid accumulation at the bottom reappears due to the increased liquid inflow. Nevertheless, the gas-liquid layer ($0.1<\varepsilon_L<0.9$) remains uniform. The increase of liquid inflow leads to an increase in the gas-liquid layer volume and contact time. This is explained by the fact that the gas-liquid drag force is lower than the centrifugal force of the liquid phase, thus increasing the gas-liquid layer volume in the chamber. Overall, it must be concluded that the values of the gas-liquid layer volume and gas-liquid contact time in the pancake-shaped chamber are higher than the values in the base case GLVU.

For the cylinder-shaped chamber, the liquid phase accumulates in the bottom plate of the chamber at Q_G = 25 m^3/h, as shown in Figures 8(f) and 7(h). When increasing the liquid flow rate from 110 kg/h (*Case* 2.I) to 330 kg/h (*Case* 2.III), the thickness of the pure liquid layer in the bottom of chamber decreases. The latter results in a decrease of the gas-liquid layer volume and contact time as compared to the base case. When increasing the gas flow rate to 75 m^3/h (*Case* 2.III), the momentum provided by the gas increases and the liquid no longer accumulates on the bottom plate of the chamber (see Figure 8(h)). However, the gas-liquid contact time becomes lower as found in Table S1. From a full comparison of the simulation results for *Cases* 1.I, 1.II, 1.III and *Cases* 2.I, 2.II, 2.III (Table S1), it is concluded that, for corresponding gas and liquid flow rates, both the gas-liquid layer volume and contact time of the pancake-shaped

chamber are higher than the values for the cylinder-shaped chamber. This is most likely explained by the fact that the low height and thus small cross-sectional area of the gas and liquid inlet slots in the pancake-shaped chamber result in very high gas and liquid injection velocities. At higher velocities the momentum input increase, resulting in a more uniform dispersion of gas and liquid in the chamber. Due to the more uniform distribution, the contact time in the pancake-shaped chamber is approximately four times longer than the contact time in the base case GLVU. When a pure liquid layer is formed on the bottom of the cylinder-shaped chamber the gas-liquid contact time is lowered, as observed when comparing *Cases* 2.I and 2.III to *Cases* 1.I and 1.III. The intensification caused by the small cross-sectional area of the gas and liquid inlet slots in *Cases* 1.I, 1.II and 1.III will result in a study of the gas-liquid inlet configuration on the gas-liquid layer volume and the gas-liquid contact time for the cylinder-shaped geometry, as discussed in sections 4.3.3 and 4.3.4.

The values of the pressure drop of *Cases* 1.I, 1.II, 1.III and *Cases* 2.I, 2.II, 2.III are presented in Table S1, while their energy consumption is depicted in Figure 8(i). It can be observed that the pressure drop in the pancake-shaped chamber is higher than that in the base case GLVU under the conditions of Q_G= 25m^3/h and Q_L=110kg/h, as well as Q_G =25 m^3/h and Q_L =330 kg/h. This is due to the fact that the thickness of the gas-liquid layer within the pancake-shaped chamber is much greater compared to the other GLVUs, requiring the gas phase to consume more energy in order to pass through the thick gas-liquid layer. However, when the gas flow rate is increased to 75 m^3/h, the pressure drop in the base case is greater than in the pancake chamber. This is due to the increased volume of the pancake-shaped chamber, which results in a decrease in the gas velocity within the chamber and a decrease in the drag force between gas and liquid, leading to a lower pressure drop. Overall, the pressure drop is impacted by a

combination of factors such as the drag force, the centrifugal force, gas-liquid layer thickness and others.

The pressure drop within the cylinder-shaped chamber is lower than the base case GLVU for all gas and liquid flow rate combinations, this is due to the cylindrical chamber having a relatively large volume. Pancake-shaped chambers have a thicker gas-liquid layer, which leads to a significantly higher pressure drop compared to cylinder-shaped chambers. This increased pressure drop results in higher energy consumption (E_{total}). Additionally, the high thickness of the gas-liquid layer in pancake-shaped chambers is an inherent property and difficult to optimize. As a result, the cylindrical chamber design is further optimized in subsequent simulations to enhance the gas-liquid contact time.

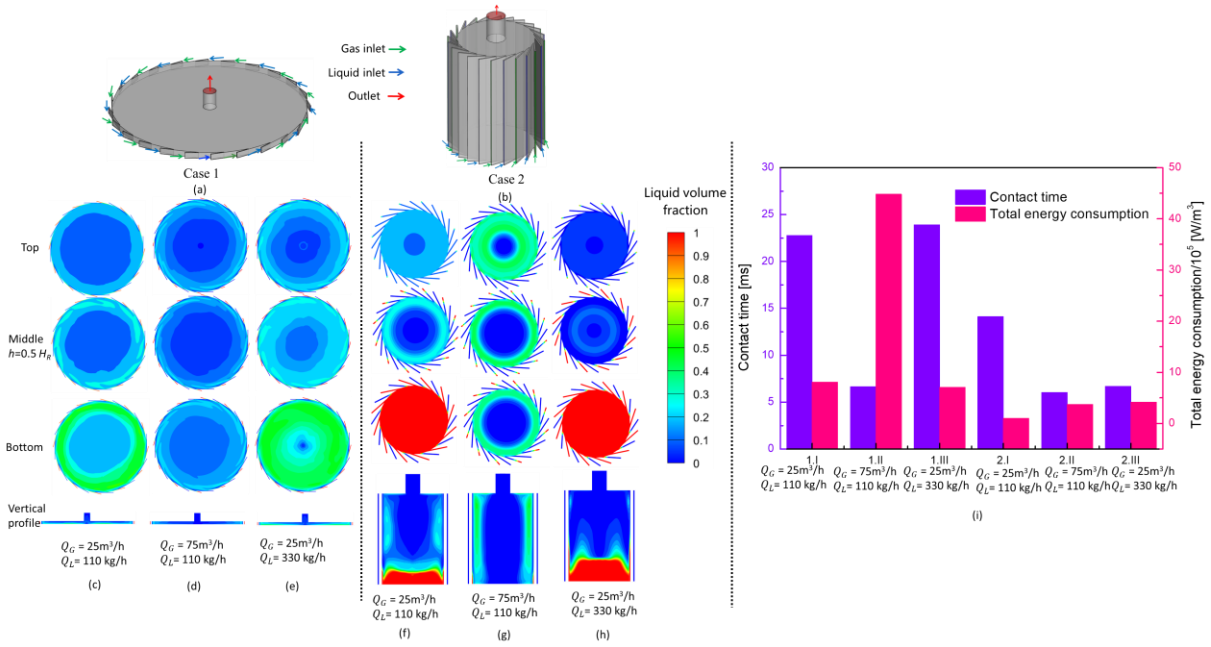

Figure 8. (a) GLVU geometry for Case 1, (b) GLVU geometry for case 2; liquid volume fraction contours for GLVUs with different shapes (c) case 1.I, (d) case 1.II, (e) case 1.III, (f) case 2.I, (g) case 2.II, (h) case 2.III; (i) gas-liquid contact time and total energy dissipation for Cases 1 and Cases 2.

4.3.2. EFFECT OF CHAMBER VOLUME (CHAMBER HEIGHT)

As discussed in section 4.3.1, possible liquid accumulation on the bottom plate of the cylinder-shaped chamber (see Figures 8(f) and (h)) results in a decrease in the gas-liquid contact time due to the non-uniformity of the gas-liquid layer. A good gas-liquid dispersion (see Figure 8(g)) can be obtained by an increase of the gas flow rate as the increased momentum transfer results in higher liquid velocities in the vortex chamber[4, 20, 25]. Some literature on gas-liquid reactor geometry optimization claims that the reactor size affects the gas-liquid velocity inside the reactor[63-65]. The cylinder-shaped chamber with a lower chamber height but with the same chamber diameter (as shown in *Case* 3 in Figure 6) is designed to study the effect of chamber volume (chamber height). It should be noted that the chamber volume of *Case* 3 is still larger than that of the *Base case*. As mentioned previously the geometry and operating condition of *Cases* 3.I, 3.II and 3.III are summarized in Table 2.

The simulation results for *Cases* 3.I, 3.II and 3.III are presented in Figures 9(b)-9(d). In Figure 9(e), the results for *Case* 2.III are added as a reference (for *Case* 3.III). A well-dispersed gas-liquid layer is formed at the outer wall of the chamber for each set of operating conditions. Due to the lower chamber volume (chamber height) as compared to *Case* 2, the injection velocity of liquid and gas increases resulting in the formation of this more uniform gas-liquid layer. This is observed when comparing Figures 9(d) and 9(e). The thick liquid layer on the bottom plate has disappeared.

The values of the gas-liquid layer volume and the pressure drop of *Case* 3.I, *Case* 3.II and *Case* 3.III are gathered in Table S1, with their gas-liquid contact time and total energy consumption illustrated in Figure 9(f). Comparing the results of *Case* 1, *Case* 3 and the *Base case* for the three sets of operating conditions, it is found that the gas-liquid layer volume and contact time

for *Case* 3 are higher than the values for the *Base case* but lower than the values for the pancake-shaped chamber (*Case* 1). It is thus concluded that an increase in the chamber volume will result in increasing the gas-liquid layer volume and contact time. The same conclusion is drawn when comparing *Case* 2.II and *Case* 3.II. By comparing the results of *Cases* 3.I, 3.III with the results for *Cases* 2.I, 2.III, the opposite conclusion is drawn. An increase of the chamber volume (chamber height) decreases the uniformity of the gas-liquid layer and thus decreases the gas-liquid contact time. Therefore, the cylinder-shaped chamber with a larger volume (higher height) (Case 2) is further optimized to obtain a well-dispersed gas-liquid layer with a higher volume. Table 2 displays the pressure drop and energy consumption for *Cases* 3.I, 3.II and 3.III. It is evident that the pressure drop and total energy consumption of *Cases* 3 are lower than those of the base case, but slightly higher than those in *Cases* 2 under all operating conditions. This is because the chamber volume in *Case* 3 is larger than the *base case* but smaller than that of *Case* 2.

When comparing the results for *Case* 3.I, *Case* 3.II and *Case* 3.III, it is concluded that a higher liquid flow rate increases the gas-liquid layer volume and contact time, as explained in section 4.3.2. Furthermore, in general, increasing the liquid phase flow rate increases the gas-liquid absorption efficiency. Thus, the operating conditions for all subsequent designs are set at a gas flow rate of 25 m^3/h and a liquid flow rate of 330 kg/h.

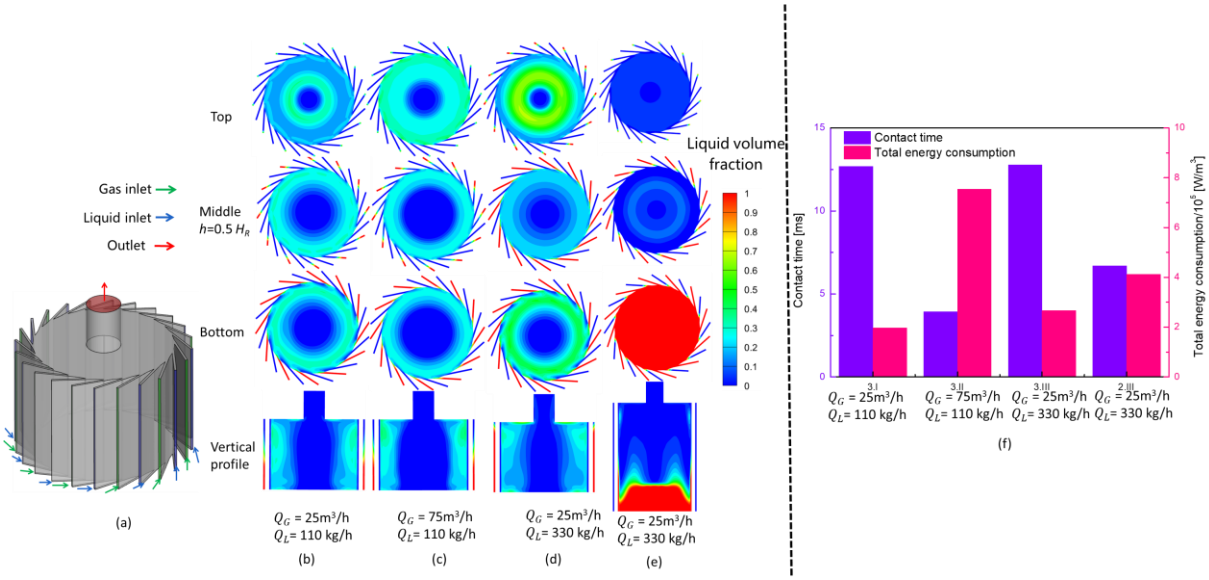

Figure 9. (a) GLVU geometry for Case 3; liquid volume fraction contours for GLVUs with different chamber heights: (b) Case 3.I, (c) Case 3.II, (d) Case 3.III, (e) Case 2.III; (f) gas-liquid contact time and total energy consumption for Cases 3 and Case 2.III

4.3.3. EFFECT OF GAS INLET HEIGHT

As mentioned in section 4.3.2, the gas and liquid inlet configurations affect the gas-liquid flow behaviors in the vortex chamber. Both the gas and liquid inlet flow provide momentum to the vortex chamber. Reducing an inlet height reduces the cross-sectional area and hence increases the initial momentum of the gas and/or liquid entering the chamber. The GLVU geometry with a partial gas inlet height is proposed in *Case* 4 (see Figure 6). Table 2 provides all dimensional information and operating conditions of the optimized GLVU for *Case* 4.

The liquid volume fraction contours for *Case* 4 are presented in Figure 10 (b). With a reduced gas inlet height, limited to the lower half of the chamber, the liquid accumulates in the top half of the chamber. Figure 10 (c) shows the contours for *Case* 2.III which is used as a reference. Results are discussed in section 4.3.1. In Figure 10 (d), the values for the gas-liquid contact time and total energy consumption for *Case* 4 are found. Due to the liquid accumulation in the bottom of the chamber (*Case* 2.III) or in the top half of the chamber (*Case* 4), the values of contact time

of *Case* 2.III and *Case* 4 are very low. A full gas inlet height is thus considered for all subsequent designs.

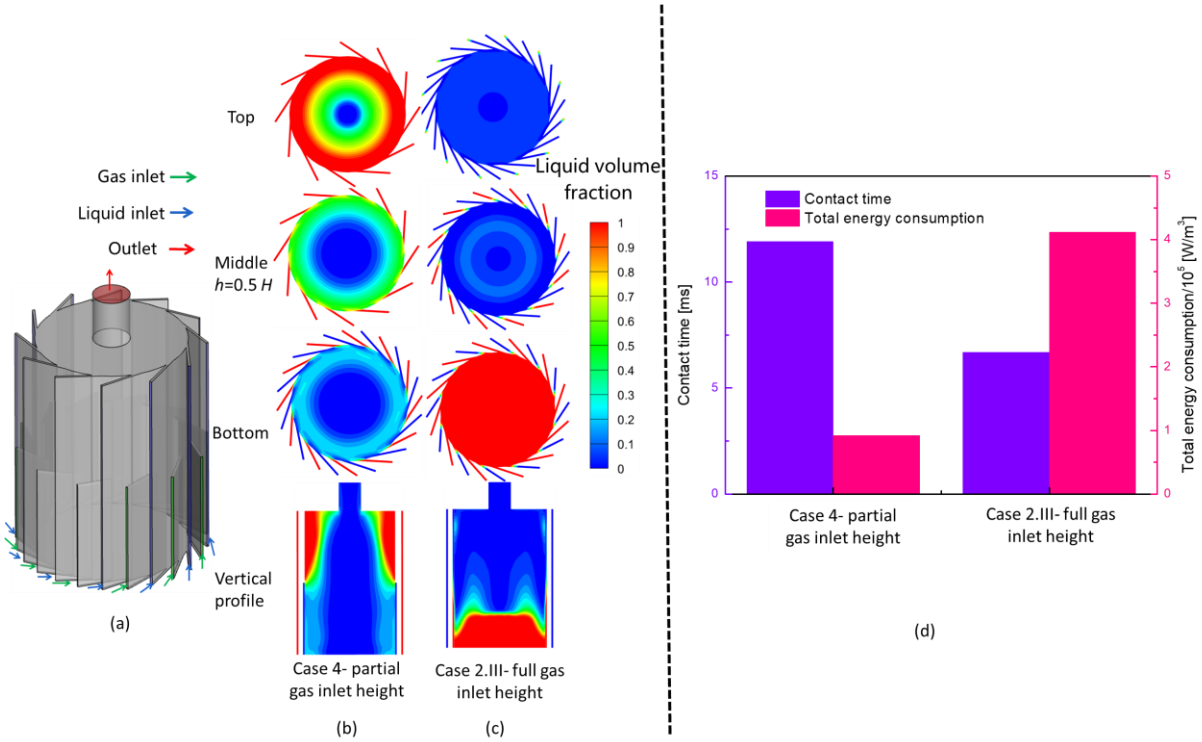

Figure 10. (a) GLVU geometry for Case 4; liquid volume fraction contours for GLVUs with different gas inlet heights: (b) Case 4, (c) Case 2.III; (d) gas-liquid contact time and total energy consumption for Case 4 and Case 2.III (Q_G= 25 m^3/h, Q_L = 330 kg/h).

4.3.4. EFFECT OF LIQUID INLET CONFIGURATION

As noted previously, the liquid inlet configuration can affect the gas-liquid flow behavior in the vortex chamber. Cylinder-shaped chambers with a partial liquid inlet height placed in different positions on the circumferential wall, as shown in *Case* 5.I, *Case* 5.II and *Case* 5.III in Figure 6, are proposed to improve the gas-liquid flow behavior.

Figure 11 displays the liquid volume fraction contours for *Case* 5.I, *Case* 5.II, *Case* 5.III and *Case* 2.III. When shifting the position of the partial liquid inlet from the top to the bottom of

the chamber, some liquid phase accumulates at the bottom of the chamber, as seen by comparing Figures 11(a) and 11(c). This observation can be explained by the limited upward rotation of the liquid phase in the chamber with a partial liquid inlet in the bottom of the chamber (see Figure 12(c)). When the partial liquid inlet is positioned in the middle of the chamber, some liquid accumulates near liquid inlets. This observation is consistent with Figure 12(b) which shows that the liquid streamlines concentrate near the liquid inlets. The latter is also observed for the liquid inlet in the bottom (see Figure 12(c)). When positioning the partial liquid inlet in the top of chamber, the liquid streamlines are evenly distributed in the vortex chamber. When the liquid inlet height is decreased from 93 mm (*Case* 2.III)(see Figure 11(d)) to 7 mm (*Cases* 5.I, 5.II and 5.III)(see Figures 11(a-c)), the liquid accumulation in the bottom of the chamber decreases, which will result in better gas-liquid contact.

Simulation results with information on contact time and total energy consumption of *Case* 5.I, *Case* 5.II, *Case* 5.III are compared in Figure 11(e). The contact time in the gas-liquid layer increases from 6.4 ms for *Case* 2.III to about 21 ms for *Case* 5.I. From this, it can be concluded that momentum input by both phases, and not by the gas phase only, has a positive effect on the GLVU operation. The latter coincides with our previous findings on the gas-liquid hydrodynamics in the vortex chamber[4, 20, 21]. With a partial liquid inlet positioned in the top of the chamber, the contact time has the highest value for *Case* 5.I. When the partial liquid inlet is shifted to a lower position, liquid accumulates on the bottom of the chamber, thus negatively influencing the contact time, as found for *Case* 5.II and *Case* 5.III. Moreover, the total energy consumption is the lowest when the liquid phase inlet is positioned at the top of the chamber. This is due to the fact that the gas-liquid layer volume is highest in this configuration, resulting in the highest liquid holdup within the chamber. Based on these simulation results, the partial liquid inlet will be placed in the top of the chamber for the next simulation.

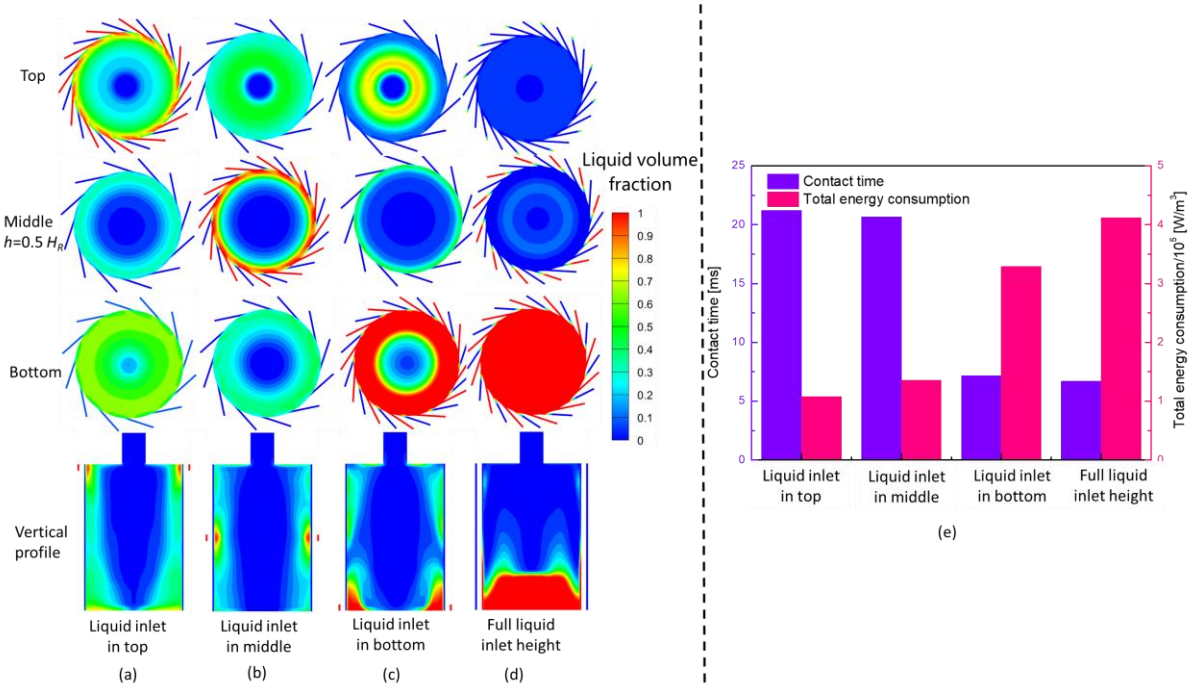

Figure 11. Liquid volume fraction contours for GLVUs with different liquid inlet position: (a) Case 5.I, (b) Case 5.II, (c) Case 5.III, (d) Case 2.III; (e) gas-liquid contact time and total energy consumption for Cases 5 and Case 2.III (Q_G= 25 m^3/h, Q_L = 330 kg/h)

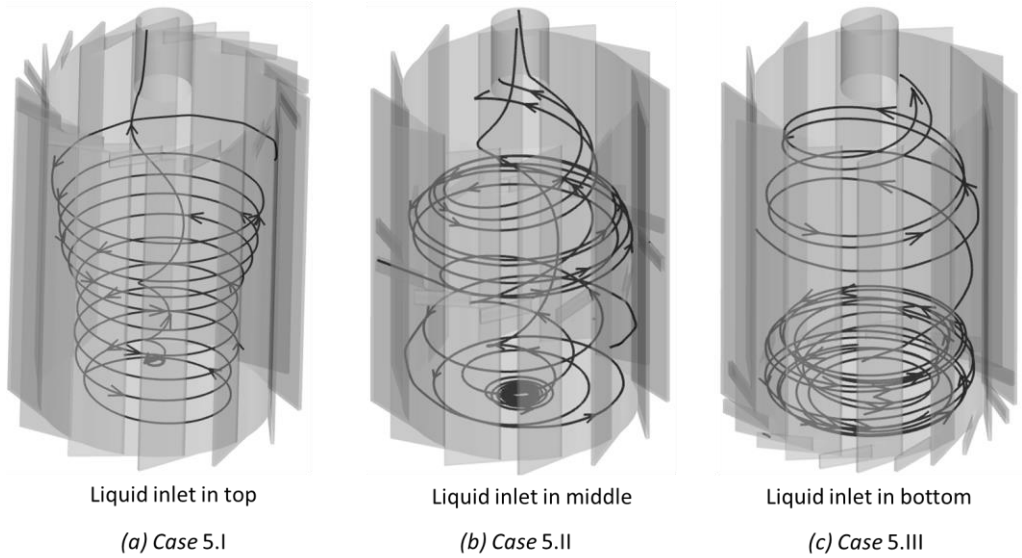

Figure 12. Liquid streamlines in the vortex chamber for Cases 5.I (a), 5.II (b) and 5.III (c), studying the effect of the liquid inlet position (Q_G= 25 m^3/h, Q_L = 330 kg/h)

4.3.5. EFFECT OF SLOT INLET WIDTH

The slot inlet width is one of the geometrical options that affect the momentum input from the gas and liquid injection. In Case 6, the inlet width of all injection inlets is decreased from 1 mm to 0.5 mm. Consequently, the gas and liquid inlet velocities are doubled, increasing the momentum input in the chamber by both phases. The effect of the inlet width on gas-liquid layer volume and gas-liquid contact time is studied by comparing *Case* 5.I and *Case* 6. Figures 13(b) – 13(c) illustrate that a uniform gas-liquid layer is formed in the chamber for both cases, with the gas-liquid contact time and total energy consumption for *Case* 6 and *Case* 5.I depicted in Figure 13(d). When comparing the contact time for *Case* 5.I and *Case* 6, similar values of about 22 ms are obtained. The latter is probably explained by the fact that for *Case* 5.I an evenly distributed gas-liquid layer at the wall is already realized. Further reduction of the inlet cross-sectional area is found to have a limited effect on the gas-liquid contact time (not shown). Additionally, the increase of gas inlet velocity caused by decreasing slot width results in a higher pressure drop in *Case* 6. This results in an increase in energy consumption. Therefore, the width of the gas-liquid inlet remains fixed at 1 mm.

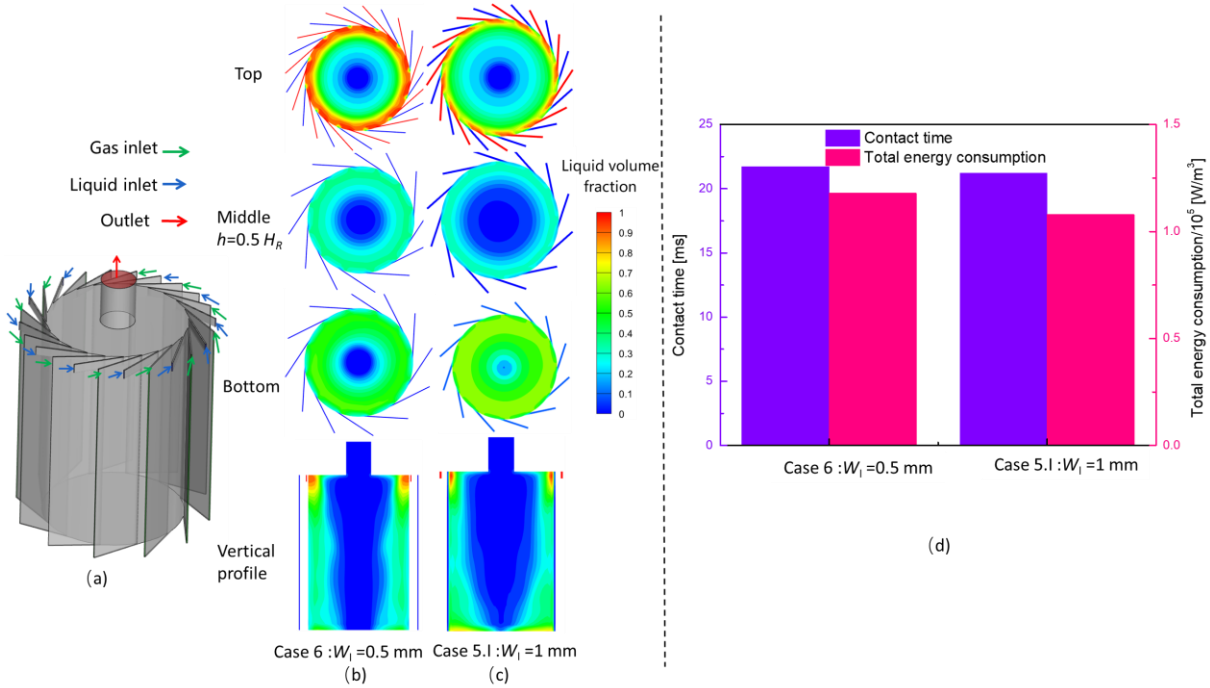

Figure 13. (a) GLVU geometry for Case 4; liquid volume fraction contours for GLVUs with different inlet widths: (b) Case 6, (c) Case 5.I; (d) gas-liquid contact time and total energy consumption for Case 6 and Case 5.I (Q_G= 25 m³/h, Q_L = 330 kg/h)

4.4. SELECTION OF CHAMBER GEOMETRY

Figure 14 compares the gas-liquid contact time for all the studied geometries and operating conditions. The contact time of *Case* 5.I is about 3 times longer than the contact time of the base case GLVU, while reducing total energy consumption by roughly 85 %. Although the total energy consumption in *Case* 1.III is significantly higher than in *Case* 5.I, it has the longest gas-liquid contact time, making it of interest for further research. Based on the simulation results, it is decided that the pancake-shaped chamber (*Case*1.III) and cylinder-shaped chamber with partial liquid inlets in the top of chamber (*Case* 5.I) will be constructed for further experimental research. In the experimental setups, the simulation results will be validated by experimental data for changing gas and liquid flow rates.

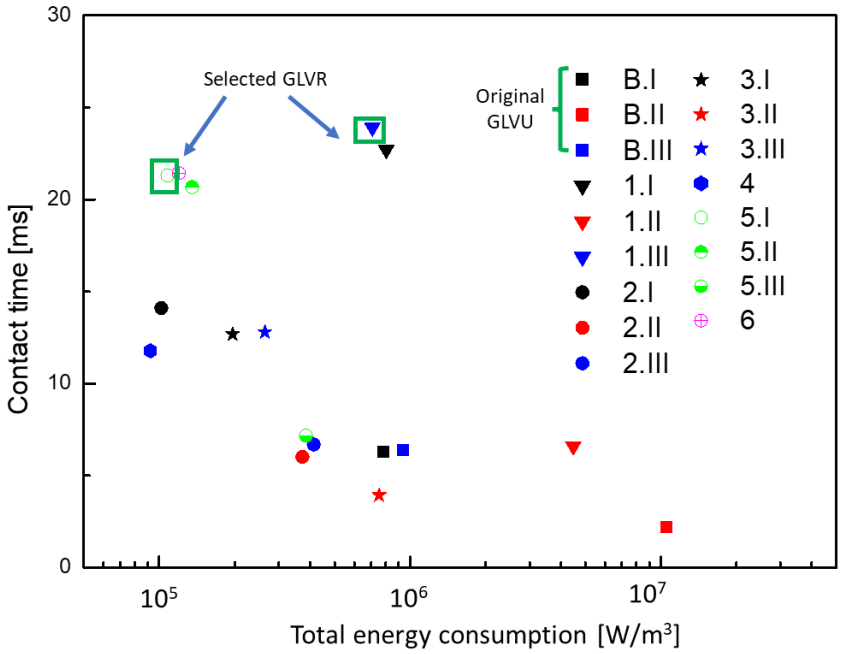

Figure 14. Gas-liquid contact time and total energy consumption for all the studied cases

In our previous study[4], the GLVU was found to exhibit a higher total energy consumption (often referred to as the energy dissipation rate[66, 67]) compared to stirred tanks, bubble columns and micro-packed beds, while aligning closely with rotor-stator spinning disc reactors. High energy dissipation rates typically denote better mixing and mass transfer characteristics, which are important for a variety of industrial applications including CO_2 capture. While these higher rates offer enhanced performance, the associated increase in operational costs must be considered as well. Achieving an optimal balance between mass transfer efficiency and cost-effectiveness is crucial. In essence, for CO_2 absorption efficiency, key elements like contact time, gas-liquid distribution, and the volumetric mass transfer coefficient play important roles. To clarify the relationship between these factors and CO_2 absorption efficiency, CFD simulations coupled to interphase mass transfer will be conducted in our future work.

5. CONCLUSIONS

In this study the gas-liquid contact time in the gas-liquid vortex reactor (GLVU) is improved by geometrical optimization using CFD. An increase of the liquid flow rate increases the gas-liquid layer volume and thus prolongs the gas-liquid contact time. Pancake-shaped chambers result in longer contact time than a cylinder-shaped chamber as the small gas and liquid inlet heights increase the injection of momentum by both phases. To realize a good gas-liquid contact in a cylinder-shaped GLVU, the gas and liquid need to be fed through a full height gas inlet and a partial height liquid inlet. Positioning the partial liquid inlet height in the top of the vortex chamber is advised. Under the selected operating conditions (G = 30 m^3/h, L = 330 kg/h), when the slot inlet width is 1 mm, a uniform gas-liquid layer can be achieved. Further reduction of the slot inlet width has a limited effect on the gas-liquid contact time. Compared to the base case GLVU design, the gas-liquid contact time is increased by a factor of 3 on average and the total energy consumption rate is reduced by 85%. A pancake-shaped chamber (D_R = 218 mm, H_R = 7 mm, H_G = 7mm, H_L = 7 mm, W_I = 1 mm) and a cylinder-shaped chamber with partial

liquid inlet in the top of the chamber (D_R = 60 mm, H_R = 93 mm, H_G = 93mm, H_L = 7 mm, W_I = 1 mm) are selected to be constructed for the experimental research of gas-liquid processes like CO_2 capture.

SUPPORTING INFORMATION

Comparison of contact time and mean gas residence time for all studied cases, table of the overview of the geometric parameters, gas-liquid layer volume, pressure drop, gas-liquid contact time and energy consumption for all studied cases, and pressure contours for GLVUs studied in this work.

NOMENCLATURE

a_1	Model constant, -
C_D	Drag coefficient, -
D_R	Chamber diameter, mm
D_ω	Cross-diffusion term, -
Eo	Eötvös number, -
E_{total}	Total energy consumption per unit liquid holdup volume, W/m^3
$\vec{F}$	The interaction force between phases
F_2	Model constant, -
G	Diffusivity term, J/(m^3·s)
g	Gravity acceleration, m/s^2
H_G	Gas inlet height, mm
H_L	Liquid inlet height, mm
H_R	Chamber height, mm
$K_{G\text{-}L}$	Interfacial momentum exchange coefficient, kg/(m^3·s)
k	Turbulent kinetic energy, m^2/s^2
ΔP	Pressure drop Pa
P	Pressure, Pa
Q_G	Gas flow rate, m^3/s
Q_L	Liquid flow rate, kg/s

q	Phase index, G or L
r	Radial position, m
r_o	Outlet radius, m
r_R	Radius of GLVU chamber, m
S	Source term, J/(m^3·s)
$S^{'}$	Strain rate magnitude, -
t	contact time, s
V_{G-L}	Gas-liquid layer volume, m^3
W_I	Inlet width, mm
W_{input}	Total energy input, W
Y	Dissipation term, J/(m^3·s)

Greek symbols

α	Volume fraction, -
α^*	Coefficient to damp the turbulent visocity, -
Γ	Generation term, -
ε	Turbulence dissipation rate, 1/s
ε_G	Average gas volume fraction in the gas-liquid layer, -
η	Molecular viscosity, kg/(m·s)
ρ	Density, kg/m^3

σ	Surface tension, N/m
σ_k	Turbulent Prandtl number for turbulence kinetic energy, -
σ_ω	Turbulent Prandtl number for specific dissipation rate, -
τ_p	Characteristic time of induced turbulence, s
$\vec{u}$	Reynolds-averaged velocity, m/s
ω	Specific turbulence dissipation rate, 1/s

Abbreviations

CFD	Computational fluid dynamics
GLVU	Gas-liquid vortex unit
GSVU	Gas-solid vortex unit
SST	Shear stress transport
VOF	Volume of Fluid

ACKNOWLEDGEMENTS

Siyuan Chen acknowledges financial support from China Scholarship Council (CSC). Yi Ouyang acknowledges financial support for a postdoctoral fellowship from Research Foundation – Flanders (FWO) grant number 1273421N. Geraldine J. Heynderickx acknowledges framework of Catalisti cluster SBO project CAPTIN (HBC.2019.0109) and CAPTIN-2 (HBC.2021.0255) within MOONSHOT innovation program. The research is funded by European Research Council (ERC) under European Union's Horizon 2020 research and

innovation program / ERC grant agreement no. 818607 (OPTIMA). Computational resources (Stevin Supercomputer Infrastructure) and services used in this work are provided by VSC (Flemish Supercomputer Center), funded by Ghent University, FWO and Flemish Government – department EWI.

REFERENCES

1. Liu, Z.; Deng, Z.; Davis, S. J.; Giron, C.; Ciais, P., Monitoring global carbon emissions in 2021. *Nat. Rev. Earth Environ.* **2022,** 3, (4), 217-219.
2. Olabi, A. G.; Abdelkareem, M. A., Renewable energy and climate change. *Renewable Sustainable Energy Rev.* **2022,** 158.
3. Florides, G. A.; Christodoulides, P., Global warming and carbon dioxide through sciences. *Environ. Int.* **2009,** 35, (2), 390-401.
4. Ouyang, Y.; Nunez Manzano, M.; Chen, S.; Wetzels, R.; Verspeelt, T.; Van Geem, K. M.; Heynderickx, G. J., Chemisorption of CO2 in a gas–liquid vortex reactor: An interphase mass transfer efficiency assessment. *AIChE J.* **2022**, e17608.
5. Ouyang, Y.; Heynderickx, G. J.; Van Geem, K. M., Development of intensified reactors: A process intensification methodology perspective. *Chem. Eng. Process.* **2022,** 181, 109164.
6. Lutze, P.; Babi, D. K.; Woodley, J. M.; Gani, R., Phenomena Based Methodology for Process Synthesis Incorporating Process Intensification. *Ind. Eng. Chem. Res.* **2013,** 52, (22), 7127-7144.
7. Wang, M.; Joel, A. S.; Ramshaw, C.; Eimer, D.; Musa, N. M., Process intensification for post-combustion CO2 capture with chemical absorption: A critical review. *Appl. Energy* **2015,** 158, 275-291.
8. Zhao, B.; Tao, W.; Zhong, M.; Su, Y.; Cui, G., Process, performance and modeling of CO2 capture by chemical absorption using high gravity: A review. *Renewable Sustainable Energy Rev.* **2016,** 65, 44-56.
9. Volchkov, E.; Dvornikov, N.; Lukashov, V.; Abdrakhmanov, R. K., Investigation of the flow in the vortex chamber with centrifugal fluidizing bed with and without combustion. *Thermophys. Aeromech.* **2013,** 20, (6), 663-668.
10. Rosales Trujillo, W.; De Wilde, J., Fluid catalytic cracking in a rotating fluidized bed in a static geometry: a CFD analysis accounting for the distribution of the catalyst coke content. *Powder Technol.* **2012,** 221, 36-46.
11. Pati, J. R.; Dutta, S.; Eliaers, P.; Mahanta, P.; Chatterjee, P. K.; De Wilde, J., Experimental study of paddy drying in a vortex chamber. *Drying Technol.* **2016,** 34, (9), 1073-1084.
12. Singh, P.; Kalita, P.; Mahanta, P.; Tamuly, P., A novel slit-less gas-solid vortex reactor dryer: Experimental validation and scale-up. *J. Taiwan Inst. Chem. Eng.* **2021,** 118, 121-130.
13. Gonzalez-Quiroga, A.; Reyniers, P. A.; Kulkarni, S. R.; Torregrosa, M. M.; Perreault, P.; Heynderickx, G. J.; Van Geem, K. M.; Marin, G. B., Design and cold flow testing of a Gas-Solid Vortex Reactor demonstration unit for biomass fast pyrolysis. *Chem. Eng. J.* **2017,** 329, 198-210.
14. Kulkarni, S. R.; Vandewalle, L. A.; Gonzalez-Quiroga, A.; Perreault, P.; Heynderickx, G. J.; Van Geem, K. M.; Marin, G. B., Computational Fluid Dynamics-Assisted Process Intensification Study for Biomass Fast Pyrolysis in a Gas–Solid Vortex Reactor. *Energy Fuels* **2018,** 32, (10), 10169-10183.
15. Vandewalle, L. A.; Van de Vijver, R.; Van Geem, K. M.; Marin, G. B., The role of mass and heat transfer in the design of novel reactors for oxidative coupling of methane. *Chem. Eng. Sci.* **2019,** 198, 268-289.

16. Vandewalle, L. A.; Marin, G. B.; Van Geem, K. M., CFD-based assessment of steady-state multiplicity in a gas-solid vortex reactor for oxidative coupling of methane. *Chem. Eng. Process.* **2021,** 165.
17. Voinov, N. A.; Zhukova, O. P.; Nikolaev, N. A., Hydrodynamics of the vortex stage with tangential swirlers. *Theor. Found. Chem. Eng.* **2010,** 44, (2), 213-219.
18. Voinov, N. A.; Zhukova, O. P.; Lednik, S. A.; Nikolaev, N. A., Mass transfer in gas-liquid layer on vortex contact stages. *Theor. Found. Chem. Eng.* **2013,** 47, (1), 55-59.
19. Deryagina, N. V.; Voinov, N. A.; Zemtsov, D. A.; Bogatkova, A. V., Hydrodynamics of the vortex tray. *Therm. Sci. Eng. Prog.* **2020,** 18, 100524.
20. Ouyang, Y.; Nunez Manzano, M.; Wetzels, R.; Chen, S.; Lang, X.; Heynderickx, G. J.; Van Geem, K. M., Liquid hydrodynamics in a gas-liquid vortex reactor. *Chem. Eng. Sci.* **2021,** 246, 116970.
21. Ouyang, Y.; Manzano, M. N.; Beirnaert, K.; Heynderickx, G. J.; Van Geem, K. M., Micromixing in a gas–liquid vortex reactor. *AIChE J.* **2021,** 67, (7), e17264.
22. Wu, S.; Zhang, L.; Sun, B.; Zou, H.; Zeng, X.; Luo, Y.; Li, Q.; Chen, J., Mass-Transfer Performance for CO2 Absorption by 2-(2-Aminoethylamino)ethanol Solution in a Rotating Packed Bed. *Energy Fuels* **2017,** 31, (12), 14053-14059.
23. Wang, B.; He, R.; Chen, M.; Pi, S.; Zhang, F.; Zhou, A.; Zhang, Z., Intensification on mass transfer between gas and liquid in fine bubble jet reactor. *J. Environ. Chem. Eng.* **2021,** 9, (1), 104718.
24. Zhang, G.; Ingham, D.; Ma, L.; Pourkashanian, M., Modelling of 3D liquid dispersion in a rotating packed bed using an Eulerian porous medium approach. *Chem. Eng. Sci.* **2022,** 250, 117393.
25. Chen, S.; Ouyang, Y.; Vandewalle, L. A.; Heynderickx, G. J.; Van Geem, K. M., CFD analysis on hydrodynamics and residence time distribution in a gas-liquid vortex unit. *Chem. Eng. J.* **2022,** 446, 136812.
26. Wu, B., Advances in the use of CFD to characterize, design and optimize bioenergy systems. *Comput. Electron. Agric.* **2013,** 93, 195-208.
27. Chen, S.; Zhang, T.; Lv, L.; Chen, Y.; Tang, S., Simulation of the hydrodynamics and mass transfer in a falling film wavy microchannel. *Chin. J. Chem. Eng.* **2021,** 34, 97-105.
28. Su, L.; Liu, Z.; Li, Y.; Xu, H.; Sun, B.; Chu, G., Structure optimization of an internal circulation rotating packed bed for the circulation liquid flow improvement: Numerical study. *Chem. Eng. Process.* **2022,** 177, 108992.
29. Pan, H.; Hu, Y. f.; Pu, W. h.; Dan, J. f.; Yang, J. k., CFD optimization of the baffle angle of an expanded granular sludge bed reactor. *J. Environ. Chem. Eng.* **2017,** 5, (5), 4531-4538.
30. Dehghani, Z.; Rahimpour, M. R.; Shariati, A., Simulation and multi-objective optimization of a radial flow gas-cooled membrane reactor, considering reduction of CO2 emissions in methanol synthesis. *J. Environ. Chem. Eng.* **2021,** 9, (2), 104910.
31. Wu, W.; Luo, Y.; Chu, G.-W.; Su, M.-J.; Cai, Y.; Zou, H.-K.; Chen, J.-F., Liquid flow behavior in a multiliquid-inlet rotating packed bed reactor with three-dimensional printed packing. *Chem. Eng. J.* **2020,** 386, 121537.
32. Li, Y.; Wen, Z.; Sun, B.; Luo, Y.; Gao, K.; Chu, G., Flow patterns, liquid holdup, and wetting behavior of viscous liquids in a disk-distributor rotating packed bed. *Chem. Eng. Sci.* **2022,** 252, 117256.
33. Zhang, W.; Xie, P.; Li, Y.; Teng, L.; Zhu, J., CFD analysis of the hydrodynamic characteristics in a rotating packed bed with multi-nozzles. *Chem. Eng. Process.* **2020,** 158, 108107.
34. Pan, Y.; Shi, Y.; Li, H.; Wang, W., Experimental and Numerical Investigations on Gas Injection-Enhanced Air Gap Membrane Distillation for Water Desalination. *Ind. Eng. Chem. Res.* **2022,** 61, (4), 1850-1862.
35. Golshan, S.; Rabiee, R.; Shams, A.; Hoballah, R.; Maheshwari, P.; Jafari, R.; Chaouki, J.; Blais, B., On the Volume of Fluid Simulation Details and Droplet Size Distribution inside Rotating Packed Beds. *Ind. Eng. Chem. Res.* **2021,** 60, (24), 8888-8900.
36. Guo, T.-Y.; Cheng, K.-P.; Wen, L.-X.; Andersson, R.; Chen, J.-F., Three-Dimensional Simulation on Liquid Flow in a Rotating Packed Bed Reactor. *Ind. Eng. Chem. Res.* **2017,** 56, (28), 8169-8179.

37. Xie, P.; Lu, X.; Yang, X.; Ingham, D.; Ma, L.; Pourkashanian, M., Characteristics of liquid flow in a rotating packed bed for CO2 capture: A CFD analysis. *Chem. Eng. Sci.* **2017,** 172, 216-229.
38. Liu, Y.; Wu, W.; Luo, Y.; Chu, G.-W.; Liu, W.; Sun, B.-C.; Chen, J.-F., CFD Simulation and High-Speed Photography of Liquid Flow in the Outer Cavity Zone of a Rotating Packed Bed Reactor. *Ind. Eng. Chem. Res.* **2019,** 58, (13), 5280-5290.
39. Zhang, W.; Xie, P.; Li, Y.; Zhu, J., Modeling of gas–liquid flow in a rotating packed bed using an Eulerian multi‐fluid approach. *AIChE J.* **2022,** 68, (4), e17561.
40. Rabiee, R.; Monzavi, M.; Shabanian, J.; Shams, A.; Golshan, S.; Jafari, R.; Blais, B.; Chaouki, J., Two-Phase flow characterization of a rotating packed bed through CFD simulation in OpenFOAM. *Chem. Eng. Sci.* **2022,** 253, 117589.
41. Lote, D. A.; Vinod, V.; Patwardhan, A. W., Computational Fluid Dynamics Simulations of the Air–Water Two-Phase Vertically Upward Bubbly Flow in Pipes. *Ind. Eng. Chem. Res.* **2018,** 57, (31), 10609-10627.
42. Babanezhad, M.; Taghvaie Nakhjiri, A.; Rezakazemi, M.; Shirazian, S., Developing Intelligent Algorithm as a Machine Learning Overview over the Big Data Generated by Euler-Euler Method To Simulate Bubble Column Reactor Hydrodynamics. *ACS omega* **2020,** 5, (32), 20558-20566.
43. Li, S.; Yang, R.; Wang, C.; Han, H.; Shen, S.; Wang, H., CFD-PBM Simulation on Bubble Size Distribution in a Gas-Liquid-Solid Flow Three-Phase Flow Stirred Tank. *ACS omega* **2022,** 7, (2), 1934-1942.
44. Anderson, T. B.; Jackson, R., Fluid Mechanical Description of Fluidized Beds. Equations of Motion. *Ind. Eng. Chem. Fundamen.* **1967,** 6, (4), 527-539.
45. Chen, H.; Sun, Z.; Song, X.; Yu, J., Key Parameter Prediction and Validation for a Pilot-Scale Rotating-Disk Contactor by CFD–PBM Simulation. *Ind. Eng. Chem. Res.* **2014,** 53, (51), 20013-20023.
46. Jain, E.; Sau, M.; Buwa, V. V., Eulerian simulations of liquid distribution generated by chimney and bubble cap distributors. *Chem. Eng. J.* **2021,** 421, 127799.
47. Zhang, Y.; Zhang, J.; Tang, Z.; Wu, Q., Regulation of gas-liquid Taylor flow by pulsating gas intake in micro-channel. *Chem. Eng. J.* **2021,** 417, 129055.
48. Shi, P.; Rzehak, R., Bubbly flow in stirred tanks: Euler-Euler/RANS modeling. *Chem. Eng. Sci.* **2018,** 190, 419-435.
49. Fleck, S.; Rzehak, R., Investigation of bubble plume oscillations by Euler-Euler simulation. *Chem. Eng. Sci.* **2019,** 207, 853-861.
50. Chen, H.; Zhang, X.-B.; Luo, Z.-H., A CFD-PBM Coupled Method to Optimize a Pilot-Scale Stirred Bioreactor. *Ind. Eng. Chem. Res.* **2022,** 61, (23), 8302-8312.
51. Zhang, H.; Guo, K.; Wang, Y.; Sayyar, A.; Wang, T., Numerical simulations of the effect of liquid viscosity on gas-liquid mass transfer of a bubble column with a CFD-PBM coupled model. *Int. J. Heat Mass Transfer* **2020,** 161, 120229.
52. Scargiali, F.; D'Orazio, A.; Grisafi, F.; Brucato, A., Modelling and Simulation of Gas–Liquid Hydrodynamics in Mechanically Stirred Tanks. *Chem. Eng. Res. Des.* **2007,** 85, (5), 637-646.
53. Moudoud, N.; Rihani, R.; Bentahar, F.; Legrand, J., Global hydrodynamic of hybrid external loop airlift reactor: Experiments and CFD modelling. *Chem. Eng. Process.* **2018,** 129, 118-130.
54. Guan, X.; Li, X.; Yang, N.; Liu, M., CFD simulation of gas-liquid flow in stirred tanks: Effect of drag models. *Chem. Eng. J.* **2020,** 386, 121554.
55. Ishii, M.; Zuber, N., Drag coefficient and relative velocity in bubbly, droplet or particulate flows. *AIChE J.* **1979,** 25, (5), 843-855.
56. Maluta, F.; Paglianti, A.; Montante, G., Experimental and numerical study of a compact inline swirler for gas–liquid separation. *Chem. Eng. Sci.* **2023,** 265, 118219.
57. Zhang, W.; Xie, P.; Li, Y.; Teng, L.; Zhu, J., 3D CFD simulation of the liquid flow in a rotating packed bed with structured wire mesh packing. *Chem. Eng. J.* **2022,** 427, 130874.
58. Putra, R. A.; Schäfer, T.; Neumann, M.; Lucas, D., CFD studies on the gas-liquid flow in the swirl generating device. *Nucl. Eng. Des.* **2018,** 332, 213-225.
59. Menter, F. R., Two-equation eddy-viscosity turbulence models for engineering applications. *AIAA journal* **1994,** 32, (8), 1598-1605.

60. Troshko, A. A.; Hassan, Y. A., A two-equation turbulence model of turbulent bubbly flows. *Int. J. Multiphase Flow* **2001,** 27, (11), 1965-2000.
61. Zhang, D.; Deen, N. G.; Kuipers, J. A. M., Numerical simulation of the dynamic flow behavior in a bubble column: A study of closures for turbulence and interface forces. *Chem. Eng. Sci.* **2006,** 61, (23), 7593-7608.
62. Vasquez, S. In *A phase coupled method for solving multiphase problems on unstructured mesh*, ASME 200 Fluids Engineering Division Summer Meeting, 2000; 2000.
63. Ansoni, J. L.; Seleghim, P., Optimal industrial reactor design: development of a multiobjective optimization method based on a posteriori performance parameters calculated from CFD flow solutions. *Adv. Eng. Softw.* **2016,** 91, 23-35.
64. Whang, K.; Shin, Y.; Baek, W.; Jo, Y.; Hwang, J. H.; Min, J.; Kim, D.; Kang, T., Direct and precise determination of volumetric mass transfer coefficient of carbon monoxide for miniaturized gas-liquid reactors via sensitive probing of raman transitions. *Chem. Eng. J.* **2022,** 429, 132260.
65. Zhao, J.; Wei, X.; Zou, J.; Zhang, Y.; Sun, J.; Liu, Z., Research on performance optimization of gas–liquid ejector in multiphase mixed transportation device. *J. Mech.* **2022,** 38, 22-31.
66. Meeuwse, M.; van der Schaaf, J.; Schouten, J. C., Multistage rotor-stator spinning disc reactor. *AIChE J.* **2012,** 58, (1), 247-255.
67. Jiang, L.; Wang, L.-H.; Liu, Y.-W.; Zou, H.-K.; Chu, G.-W.; Luo, Y., HiGee Microbubble Generator: (I) Mathematical Modeling and Experimental Verification of the Energy Dissipation Rate. *Ind. Eng. Chem. Res.* **2022,** 61, (45), 16823-16831.

Graphical abstract: